Mechanical Properties of Bone-Shaped-Short-Fiber Reinforced Composites

Y.T. Zhu, J A. Valdez, I.J. Beyerlein, S.J. Zhou*, C. Liu
M.G. Stout, D.P. Butt, and T.C. Lowe

Materials Science and Technology Division, MS G755
*Applied Physics Division, MS B258
Los Alamos National Laboratory, Los Alamos, NM 87545

Acta Materialia (in press), LAUR# 98-5326

Abstract

Short-fiber composites usually have low strength and toughness relative to continuous fiber composites, an intrinsic problem caused by discontinuities at fiber ends and interfacial debonding. In this work, we fabricated a model polyethylene bone-shaped-short (BSS) fiber reinforced polyester-matrix composite to prove that fiber morphology, instead of interfacial strength, solves this problem. Experimental tensile and fracture toughness test results show that BSS fibers can bridge matrix cracks more effectively, and consume many times more energy when pulled out, than conventional straight short (CSS) fibers. This leads to both higher strength and fracture toughness for the BSS-fiber composites. A computational model was developed to simulate crack propagation in both BSS and CSS-fiber composites, accounting for stress concentrations, interface debonding, and fiber pullout. Model predictions were validated by experimental results and will be useful in optimizing BSS fiber morphology and other material system parameters.

1. Introduction

Engineered composite materials are well known for their superior properties. For instance, fiber-reinforced composites have superior mechanical properties over their unreinforced matrix. For civilian applications, cost is often a deciding factor in materials selection. Compared with continuous fiber composites, short-fiber composites are cost effective because they can be adapted to conventional manufacturing techniques [1-6]. However, the application of short-fiber composites has so far been limited primarily to light-load-bearing components, because of their low strength and toughness.

The relatively low strength and toughness of short fiber composites are intrinsic problems caused by two main factors. First, numerous discontinuities provided by fiber ends can produce stress concentrations on nearby fibers and promote matrix microcracking at these ends. These microcracks, which occur even prior to fiber failure, most likely coalesce to form a large main crack. Second, the fiber/matrix interface is often a limiting factor for improving mechanical properties of short fiber composites [7-10]. With respect to interface selection, there exists a trade off between the strength and toughness of short-fiber composites: high strength is often obtained at the sacrifice of toughness. For a short fiber composite, a strong interface is desirable to transfer load from matrix to fibers, since relatively stronger interfaces can increase the effective fiber length over which the fiber carries load [11-13]. However, strong interfaces and nearby fiber ends can produce stress concentrations which induce fiber failure rather than fiber bridging and pull-out, particularly in response to an approaching crack

[14,15]. Even for composites with highly ductile matrices, such as metal and polymer matrices, strong interfaces will promote successive breakage of adjacent fibers [15,7], and interfacial debonding and matrix crack bridging are not dominating failure mechanisms [16]. Weak interfaces, on the other hand, can reduce stress concentrations in a short fiber by debonding. However, they also significantly decrease the effective length of the fiber that carries load, rendering the fiber ineffective in strengthening the matrix. Extremely weak interfaces may result in *complete* fiber interfacial debonding and pullout, producing a significant loss in composite strength with no or minimal improvement in composite toughness.

A new concept to overcome the interface problem of short-fiber composites has been recently reported: fiber morphology design [17,18]. In previous work [17], short fibers were designed to have two enlarged ends. Because of the resulting appearance, these fibers were called bone-shaped short (BSS) fibers. BSS fibers can effectively transfer load from the matrix to the fiber at the two enlarged ends by matrix-fiber interlocking. As a result, a weak interface can be used to allow easy interfacial debonding and to reduce stress concentrations, but without compromising fiber-matrix load transfer. Composites reinforced with BSS fibers have been reported to have higher strength and higher stiffness, but lower strain-to-failure [17]. In this work, we have further studied the strength and fracture behavior of these BSS-fiber composites, as well as the crack-bridging capability and pull-out resistance of BSS fibers.

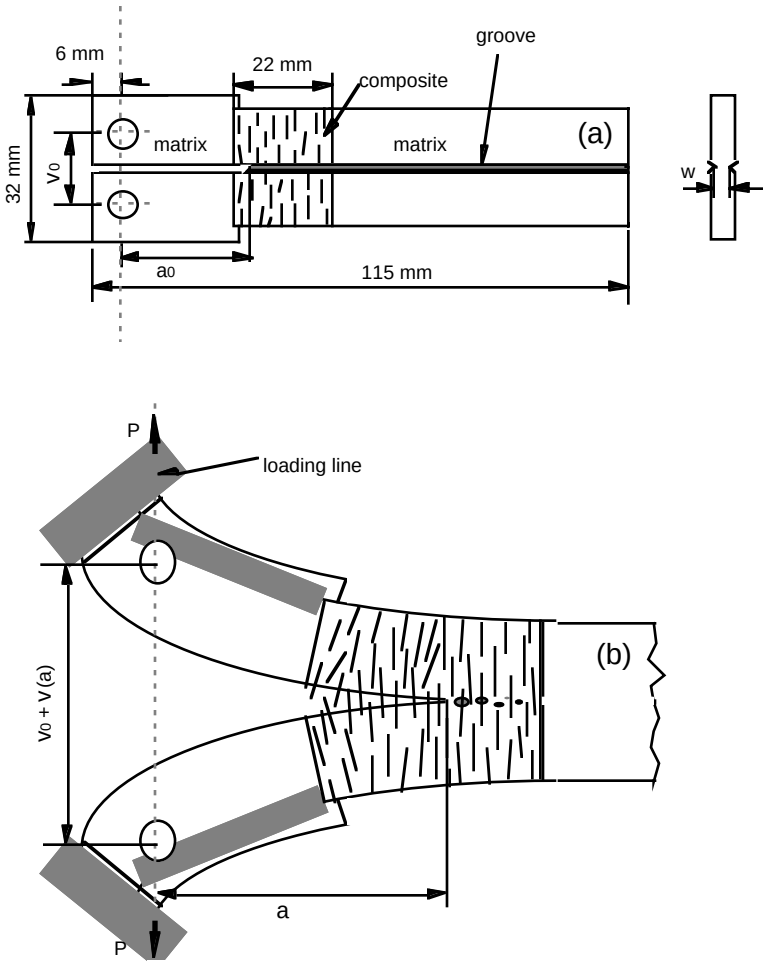

Fig. 1 A sketch of (a) an undeformed DCB specimen and (b) a deformed DCB specimen.

The effectiveness of these BSS fibers for different composite material systems can be predicted using computational micromechanical modeling which simulates crack propagation and macroscopic response. In this study, a computational model was developed and simulations were carried out to study the effect of the BSS fiber morphology on crack-bridging and fracture resistance. In particular, the influences of random variations in fiber location and stress concentrations, caused by nearby fiber ends, on crack propagation were accounted for.

In this paper, we first describe the experimental procedure and compare the BSS-fiber composite strength and toughness results with that of conventional straight short (CSS) fiber

composites. We then follow with development of a computational model and its predictions and close with implications of our results and future work.

2. Experimental Procedure

Continuous commercial polyethylene (Micro Dyneema^{TM}) fibers with diameter d = 160 μm and Young's modulus E = 68.5 GPa were used to manufacture both the BSS- and CSS-fiber composites. The BSS fibers were processed using a small hydrogen torch which severed the fiber and caused the polyethylene to 'bead' up at the ends [17]. As a result, the enlarged ends of the BSS fibers looked like mushroom caps. The CSS fibers were precisely cut using a pair of scissors. In bulk, the Young's modulus E_m and shear modulus G of the matrix were measured as ~500 MPa and ~170 MPa, respectively.

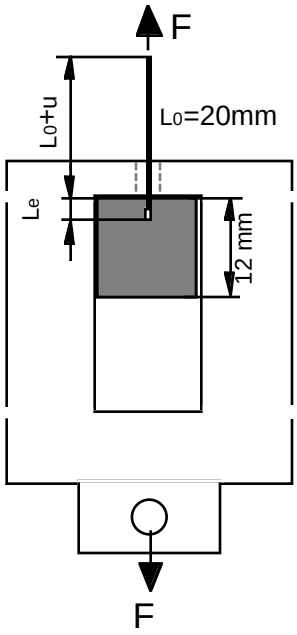

Fig. 2 A sketch of single-fiber pullout testing. The fiber is embedded in the matrix for a length of L_e, and its unembedded length is 20 mm. The matrix is in cubic shape with each edge = 12 mm.

Tensile test specimens of short-fiber reinforced polyester matrix were fabricated with short-fibers well aligned in the longitudinal (loading) direction [17]. The matrix was thickened with amorphous fumed silica so as to suspend the fibers in the matrix before curing. Readers are referred to [17] for more details on the fabrication of these tensile composite specimens. Double cantilever beam (DCB) samples were also fabricated to measure the crack resistance of the composites (Fig. 1a). The short fibers were oriented perpendicular to the precrack and as in the tensile specimen, were well aligned. Because of the difficulty in fabricating a whole DCB specimen with aligned fibers, only the section of the specimen immediately ahead of the precrack was composite while other parts were matrix. The tip of the precrack was sharpened with a blade before testing. As shown in Fig. 1a, a groove was machined on both sides of the specimen to prevent the crack from deviating from the line of symmetry. For both the BSS- and CSS-fiber composites, the tensile specimens were fabricated with ℓ = 3.0 and 4.5 mm short fiber lengths and the DCB specimens with ℓ = 3.0 mm fiber lengths. The fiber volume fraction in all specimens was approximately 5%. Fiber volume fractions and fiber lengths were limited to these values by the curing and alignment procedures [17].

Single-fiber pullout tests were also performed to compare the pull-out resistance and consumed energies of the BSS and CSS fibers and to estimate fiber-matrix interfacial strength for subsequent modeling. The sample dimensions and testing rig are shown in Fig. 2. The embedded lengths L_e were chosen as 3.5 mm and 6.4 mm.

All composite samples were fabricated using the same matrix material and allowed to cure in air at room temperature for seven days before mechanical testing, in order to attain a consistent matrix properties. All mechanical tests were conducted using a Model 1125 Instron testing machine. For tensile testing, an extensometer with a gage length of one inch was used to measure the strain, and a constant strain rate of 1×10^{-4} s^{-1} was applied. For DCB testing, an LVDT was used to measure the crack opening, while a traveling microscope was used to measure the *in situ* crack length. Fracture surfaces were investigated using a JEOL 6300FXV Scanning Electron Microscope (SEM).

3. Experimental Results and Discussions

3.1 Tensile Properties

In Fig. 3 are pictures of (a)-(c) BSS-fiber and (d) CSS-fiber reinforced composite specimens during tensile testing. Figure 3a shows that at 5% strain, the surface of the BSS-fiber reinforced composite specimen became rough. The rough surface was caused by the non-uniform stress state of the polyester matrix as a result of the spatial variation in the location of the fibers. In the failure process, some of the BSS fibers contributed to forming the crack and some contributed to bridging the crack and eventually were pulled-out. Matrix crack formation was found to be more likely in regions where several ends were roughly aligned along a plane perpendicular to the straining direction. The arrow in Fig. 3a indicates such a weak cross-section of high local stress concentration, appearing as a linear surface groove across the specimen surface.

Upon further straining, a matrix crack was initiated at this site (Fig. 3b), but was effectively bridged by BSS fibers to prevent catastrophic failure of the specimen. The surface area directly above and below the crack is smooth due to stress relaxation in these areas, while the surface away from the crack is rather rough. As the specimen was further strained, it became bent as the main matrix crack propagated in a stable manner from left to right with BSS fibers pulling-out in its wake, and a second matrix crack developed (see arrow in Fig. 3c). In contrast, CSS fibers could not as effectively bridge the matrix crack, resulting in immediate pull-out and sample failure once a matrix crack formed (Fig. 3d). In both cases, the fibers did not fracture, composite strength was dominated by matrix crack initiation at fiber ends, and fiber bridging and pull-out.

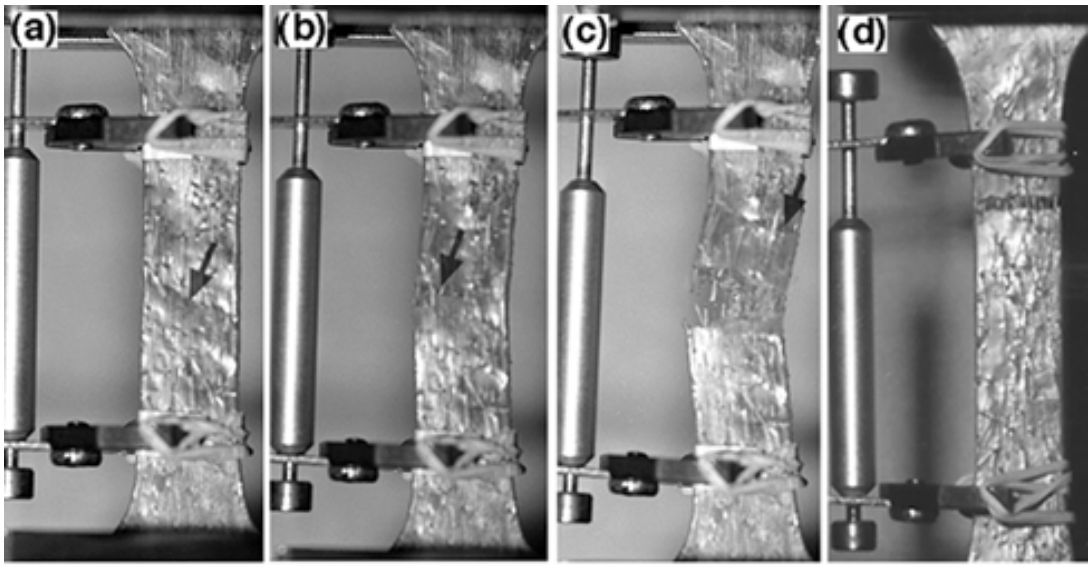

Fig. 3 *In situ* pictures of (a) - (c) BSS-fiber reinforced and (d) CSS-fiber reinforced tensile specimens during tensile testing. The engineering strain states are (a) 5%, (b) 13%, (c) 20% and (d) 25%.

What we have discussed above is the macroscopic observation of the tensile failure process of BSS- and CSS-fiber composites. More insightful information can be obtained from microscopic fractographs of these composites (Figs. 4 and 5). For the BSS-fiber composites, the crack usually initiated at fiber ends (Fig. 4a), or at surface flaws on the specimen (see arrow in Fig. 4b). The main crack propagated by coalescing with small cracks formed at nearby BSS-fiber ends. The smaller cracks were often not on the same plane as the larger crack, resulting in a very rough fracture surface. Because of the processing technique used in this study, the ends of BSS fibers were usually disk-shaped, with their broad face perpendicular to the longitudinal axis of the fiber. When a composite specimen was loaded in tension, each fiber end acted much like a crack oriented perpendicular to the loading direction. Though the bulk polyester matrix can sustain relatively large deformations, as shown by the matrix stress-strain curves in Fig. 6, the complex, triaxial stress state of the matrix material in the composite makes the matrix crack sensitive. When a matrix crack is initiated at a fiber end, the polyester matrix behaves in a brittle manner, as evidenced by the river-marks in fractographs of both BSS- and CSS- fiber composites (Figs. 4 and 5, respectively). These river-marks are similar to that on the fractured surface of a typical brittle ceramic material. As a crack propagates, some BSS fibers bridging the crack might be pulled out, which is a difficult process because of the enlarged ends. The pullout process consumed large amounts of energy, since it resulted in extensive damage to the matrix (Fig. 4c).

Figure 5 shows the fractographs of several CSS-fiber composite samples. Figure 5a shows a fracture surface which formed from a crack initiated at a fiber end (see the arrow mark). The small crack propagated slowly at the beginning, leaving a smooth mirror-like area. Once the crack grew to a critical size, it propagated quickly across the whole specimen, leaving a relatively flat fracture surface with river marks. Figure 5b shows a case of initial crack formation from clustered fiber ends (see arrows in the figure). No smooth mirror zone associated with slow crack propagation can be seen, apparently because the crack grew to an unstable size by coalescence of several small cracks. Once the crack reached a critical size, it propagated through the entire cross- section of the sample, pulling out fibers in its wake. It can be seen from the river marks that the sample failed from a single crack (Fig. 5b). This is consistent with the observation in Fig. 3 that the crack propagated quickly after its formation. In contrast to BSS fibers, the pullout of CSS fibers did not result in much matrix damage (Fig. 5c), which means less energy was consumed during the pullout process.

The different failure processes of the BSS- and CSS-fiber composites have a significant effect on their mechanical response under tensile loading, as revealed in the strain-stress curves shown in Fig. 6. The maximum strengths measured for each sample are indicated by the circles on these stress-strain curves and are also listed in Table I. Firstly, despite the relatively small volume fraction V_f and short fiber length ℓ, these BSS fibers were extremely effective in strengthening the bulk matrix material. Secondly, the average strengths of the BSS-fiber composites are greater than CSS-fiber composites by 11.1% and 22.4% for samples with ℓ = 3.0 and 4.5 mm, respectively. The strengths of both BSS- and CSS-fiber composites should approach the strength of continuous fiber composites as ℓ increases further, and likewise, approach the strength of particulate-reinforced composites as ℓ decreases. Therefore, although the difference in strength between the BSS- and CSS-fiber composites may continue to increase (as shown in Table I), it will eventually decrease with increasing ℓ. In other words, we expect there exists an optimum ℓ at which BSS-fiber composites will have the largest improvement in strength over CSS-fiber composites for a

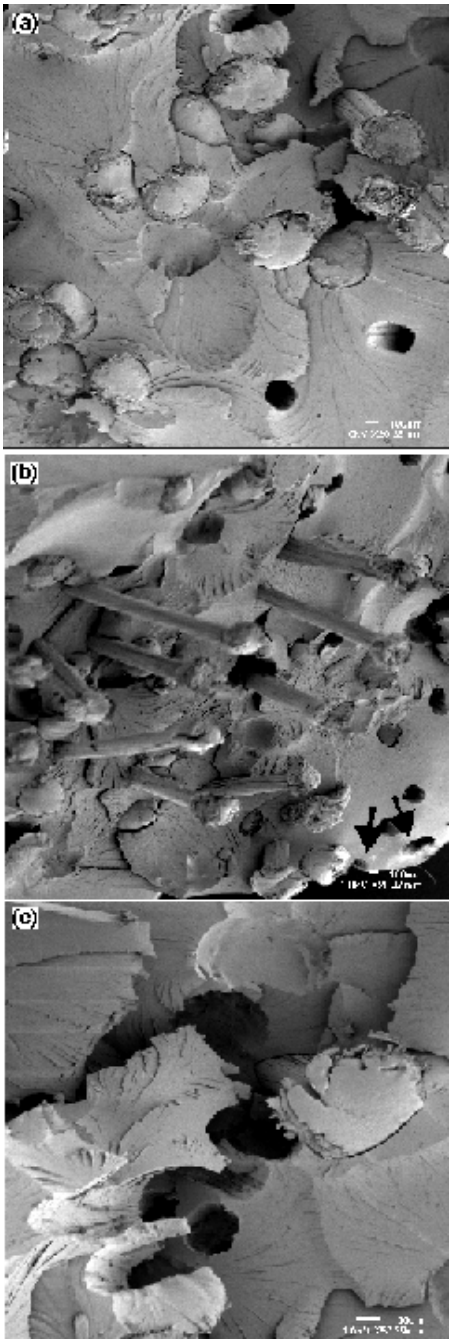

Fig. 4 SEM micrographs of fracture surfaces of BSS-fiber composites.

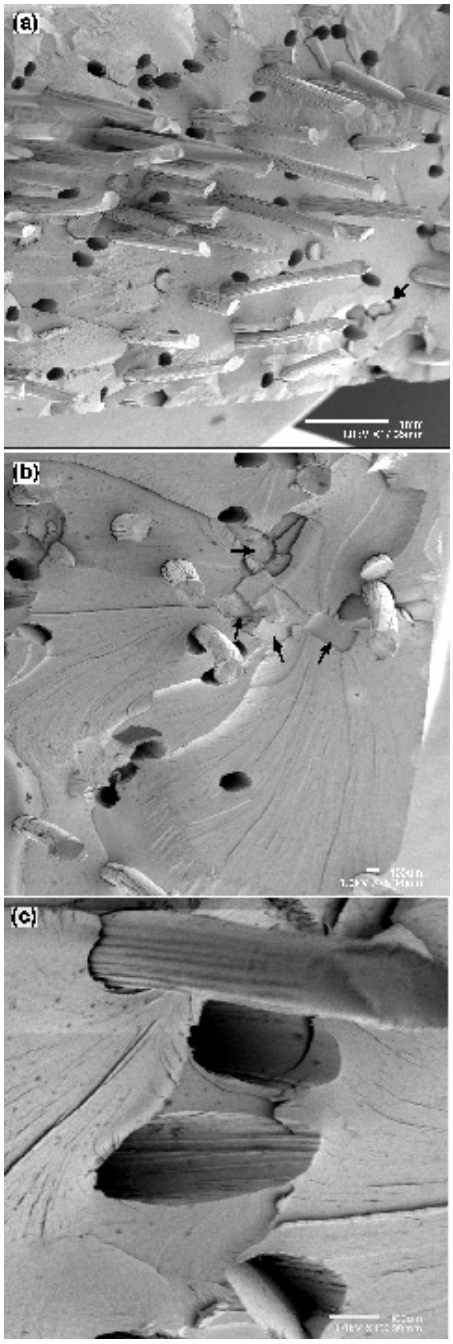

Fig. 5 SEM micrographs of fracture surfaces of CSS-fiber composites.

Table I. The maximum strengths of the BSS- and CSS- fiber composites (fiber length ℓ = 3.0 and 4.5 mm, respectively). The matrix stress at the circle on the stress-strain curve is 11.5 MPa.

Sample #	Composite strength σ_c (MPa)			
	ℓ = 3.0 mm		ℓ = 4.5 mm	
	BSS	CSS	BSS	CSS
1	14.6	13.7	16.7	13.8
2	14.8	13.5	16.0	13.3
3	14.8	12.3	16.5	13.0
Average	14.7	13.2	16.4	13.4

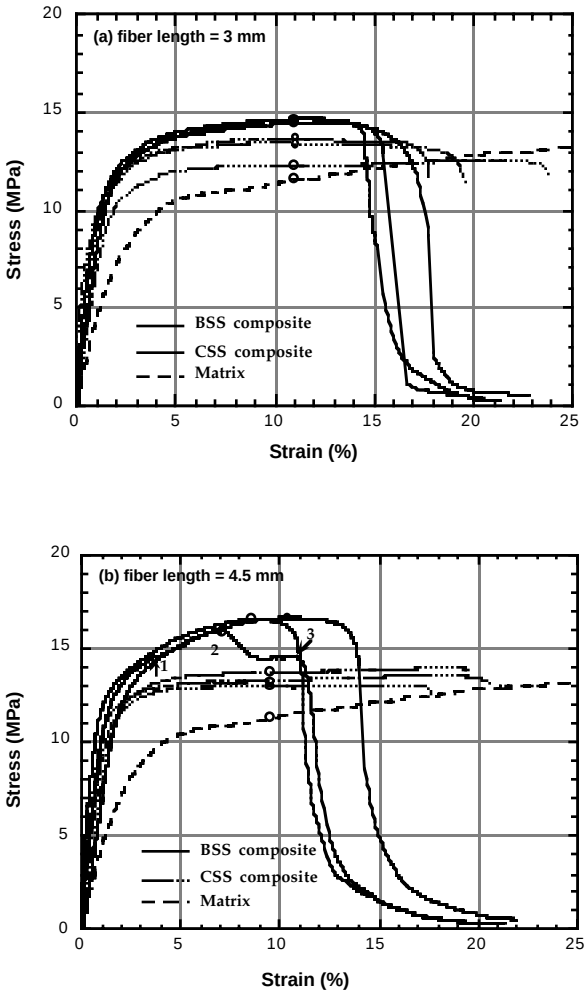

Fig. 6 Stress-strain curves of BSS- and CSS-fiber composites and polyester matrix for (a) ℓ = 3 mm and (b) ℓ =4.5 mm.

given material system. This value of ℓ will be related to a critical length at which statistical fiber strength, rather than the density and distribution of fiber ends and fiber length ℓ, begins to govern composite strength and pull-out lengths.

One salient feature of the strain-stress curves of BSS-fiber composites is the gradual stress decrease with increasing strain at composite failure. This is in sharp contrast to the strain-stress curves of the CSS-fiber composite, in which the stress suddenly dropped to zero at composite failure. This is consistent with the observations seen in Fig. 3 that cracks propagated in a stable manner in the BSS-fiber composites, but cause catastrophic failure the CSS-fiber composites. This reduced crack sensitivity of the BSS-fiber composites is provided by the effective crack-bridging capability of the enlarged BSS fiber ends. One of the strain-stress curves of BSS-fiber composites in Fig. 6b shows three abrupt stress drops (see arrows). The first drop occurred at 3.5% strain, which was probably caused by the initiation of a crack. Afterwards, the composite sample was able to sustain higher stresses at larger applied strains due to the effective crack-bridging of BSS fibers. The second stress drop at 7% strain was caused by either the formation of a new crack or

sudden propagation of an existing crack. The stress plateau following the second stress drop suggests that the crack was also effectively arrested by BSS fibers. Finally at 11% strain, the BSS fibers could no longer prevent the propagation of the large crack, which led to a gradual stress decrease with increasing strain.

3.2 Effective Stress Analysis

The benefit of BSS fibers is also revealed when considering a simple "effective fiber stress" analysis using data from Table 1. In this analysis, these composite samples can be approximately considered as reinforced by unidirectional short fibers. (Interested readers are referred to [19,20] for more accurate analyses for the 3D non-symmetric fiber orientation function from 2D image analyses and the strength of short fiber composites whose fiber orientation can be described by an orientation function.) The average fiber stress at maximum composite strength, σ_{ef}, can be approximated from a simple rule-of-mixtures [21,16] as

$$\sigma_{ef} = \left[\sigma_c - \left(1 - V_f\right)\sigma_m\right] \Big/ V_f \qquad (1)$$

where σ_c is the maximum strength of the composites (See Table 1), V_f is the fiber volume fraction, and σ_m is the stress in matrix at which the maximum composite strength is measured (see Fig. 6 and Table 1).

In both the BSS- and CSS-fiber composites, V_f and ℓ were the same; however, their σ_{ef} must be interpreted differently. For a BSS fiber, σ_{efb} is the average stress along the fiber, assuming ℓ equals the volume of the fiber divided by its cross-section. This assumption slightly overestimates the actual ℓ of the BSS fiber because of the volume associated with its enlarged ends. For the same ℓ, a BSS fiber has a larger volume than a CSS fiber because of its enlarged mushroom-shaped ends. Also, the larger volume of the BSS fibers leads to a smaller number of fibers per unit volume in BSS-fiber composites than in CSS-fiber composites for the same V_f, as is the case in this study. So given α, the volume ratio of a BSS fiber to a CSS fiber, the relationship between the actual effective fiber stress, σ^a_{efb}, and σ_{efb} can be expressed as

$$\sigma^a_{efb} = \alpha\sigma_{efb} \qquad (2)$$

For the polyethylene fibers used in this study, α = 1.27 for ℓ = 3 mm and α = 1.18 for ℓ = 4.5 mm and thus, σ^a_{efb} is larger than σ_{efb} calculated by Eq. 1.

Using the average maximum strength data from Table I, the effective fiber stress, σ_{efb}, and actual effective fiber stress, σ^{a}_{efb}, for the BSS-fiber composites and the effective fiber stress, σ_{efc}, for the CSS-fiber composites, are calculated using Eqs. 1 and 2, and listed in Table II. It can be seen that the ratio of effective fiber stress in BSS fibers to that in CSS fibers, $\sigma_{efb}/\sigma_{efc}$, is 1.72 when ℓ = 3.0 mm, and increases to 2.19 when ℓ = 4.5 mm. The ratio $\sigma^{a}_{efb}/\sigma_{efc}$ is 2.18 when ℓ = 3.0 mm, and increases to 2.58 when ℓ = 4.5 mm. In other words, a BSS fiber with the geometry used in this study is 118% more effective than a CSS fiber in improving composite strength when ℓ = 3.0 mm, and 158% more effective when ℓ = 4.5 mm.

Table II. The effective fiber stress, σ_{efb}, actual effective fiber stress, σ^{u}_{efb}, for BSS-fiber composites and the effective fiber stress, σ_{efc}, for CSS-fiber composites, as calculated using Eqs. 1 and 2.

Fiber length ℓ	ℓ =3.0 mm	ℓ =4.5 mm
σ_{efb} (MPa)	71.7	116.5
σ^{a}_{efb} (MPa)	91.1	137.4
σ_{efc} (MPa)	41.7	53.3
$\sigma_{efb}/\sigma_{efc}$	1.72	2.19
$\sigma^{a}_{efb}/\sigma_{efc}$	2.18	2.58

There are two important factors of this effective stress analysis that we should note. First, in Eq. 1, σ_{ef} is considered as the average stress along the fiber and among all the fibers. However, the stress distribution along the fiber length is not uniform [22], especially when considering stress concentrations produced by nearby fiber ends. Secondly, fibers in our tensile samples did not fracture but instead pulled-out during the failure process. This suggests that the load transfer length was comparable or less than the fiber length. In theory, this load transfer length ℓ_c is estimated as [21,16],

$$\ell_c = \sigma_0 r/2\tau_y \tag{3}$$

In the case that $\ell < \ell_c$, the rule of mixture can be expressed as [16],

$$\sigma_c = V_f\left(\frac{\tau_y l}{2r}\right) + V_m\sigma_m \tag{4}$$

which implies that τ_y = 4.03 MPa and 3.89 MPa for the BSS ℓ = 3.0 and 4.5 mm fibers and τ_y = 2.43 MPa and 1.76 MPa for the CSS ℓ = 3.0 and 4.5 mm fibers. Thus, the effect of the BSS fibers are accounted for in Eq. 4 by a higher sliding resistance. However, Eq. 3 assumes that the fiber strength, σ_0, is equal among fibers; stress concentrations are negligible, and the interface sliding shear stress, τ_y, is constant. Thus, considering stress concentrations produced by nearby fiber ends and randomly occurring weak fiber flaws, it is possible that fibers with lengths below the ℓ_c predicted by Eq. 3 can fracture. (The strength of these flaws which

govern fiber strength have been shown to follow a Weibull distribution for polyethylene fibers having a wide range of fiber diameters and fiber moduli [23].) Predicting ℓ_c is important since the increase in the BSS fibers will be more effective when most of the fibers do not fracture. For these reasons, computational modeling which can simulate all these synergistic effects and potentially predict ℓ_c is considered later.

3.3 Crack Propagation Resistance

In order to investigate the fracture toughness of the CSS-fiber composites and BSS-fiber composites and crack-bridging effectiveness of the BSS fibers, DCB samples (Fig. 1) were fabricated and tested. Figure 7 shows the curves of normalized load, $\overline{P}$, against crack length, a, for both BSS- (solid marks) and CSS-fiber composites (open marks) with ℓ = 3 mm. The normalized load was calculated as $\overline{P}=P/w$, where P is the measured load and w is the crack width (see Fig. 1a). The crack length, a, was measured *in situ* as the distance between the loading line and the crack tip (Fig. 1b). It is clear from Fig. 7 that higher load is required to propagate cracks in the BSS-fiber DCB specimens than in the CSS-fiber DCB specimens. This further proves that BSS fibers bridge cracks more effectively than CSS fibers.

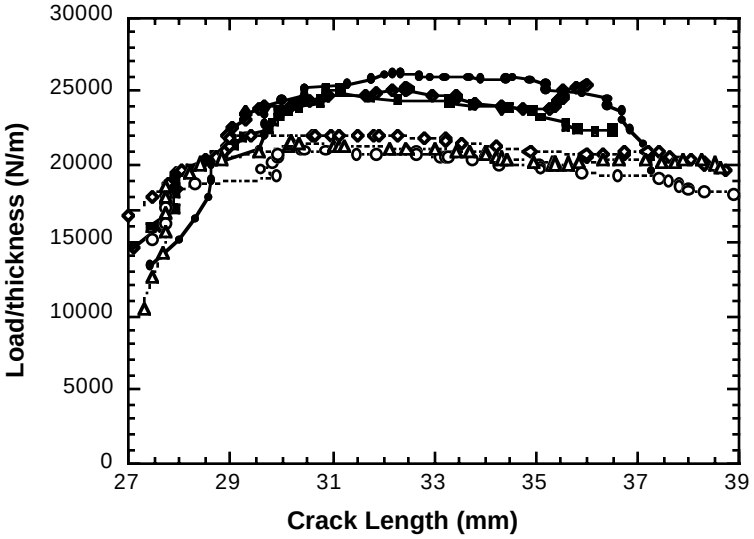

Fig. 7 The crack length-load curves obtained from DCB tests of BSS- and CSS-fiber composites (ℓ = 3 mm, see Fig. 3 for specimen geometry). The solid markers represent data points for BSS-fiber composites and the hollow markers represent data points for CSS-fiber composites.

The total normalized energy consumed for a crack to propagate from the initial crack length a_0 to crack length a can be calculated as

$$E(a)=\int_0^{v(a)}\overline{P}(v)dv \qquad (5)$$

where $\overline{P}$ (v) is the normalized load as a function of crack opening displacement, $v(a)$, along the loading line (See Fig. 1). Each measured crack length, a, corresponds to a displacement, $v(a)$. Shown in Fig. 8a are the total normalized energies, $E(a)$, calculated by Eq. 5, as a function of crack length for DCB tests of both BSS- and CSS-fiber composites. As shown, $E(a)$ is higher for BSS-fiber composites than for CSS-fiber composites.

The supplied energy for a crack to propagate by a unit length can be calculated by

$$\varepsilon(a)=\frac{dE(a)}{da} \qquad (6)$$

This can be done by first fitting the curves in Fig. 8a of $E(a)$ versus a with a polynomial function and then obtaining its derivative. As shown in Fig. 8a, $E(a)$ values from an individual

DCB testing is not a smooth function of crack length and vary substantially from specimen to specimen, as a result of the random distribution of fibers bridging the crack. Therefore, for fitting purposes, we combined all three data sets of $E(a)$ for each type, BSS- and CSS-fiber composites, to fit them to a third order polynomial function (see Fig. 8a).

Using Eq. 6, $\varepsilon(a)$ was calculated from this polynomial function and is shown in Fig. 8b. For both types of DCB specimens, $\varepsilon(a)$ is an increasing function of a. Also note that $\varepsilon(a)$ includes energies consumed both by crack propagation and by further deformation in the two beams of the DCB specimen, which makes it larger than the crack resistance, R, or the energy consumption in the formation of a unit length of crack [24]. As shown, the BSS-fiber DCB specimens require significantly more energy for crack propagation than the CSS-fiber DCB specimens. Since the fibers did not fracture, this enhanced crack resistance, or indirectly, higher fracture toughness of the BSS-fiber composites, is due solely to their enhanced ability to bridge matrix cracks and to resist pull-out.

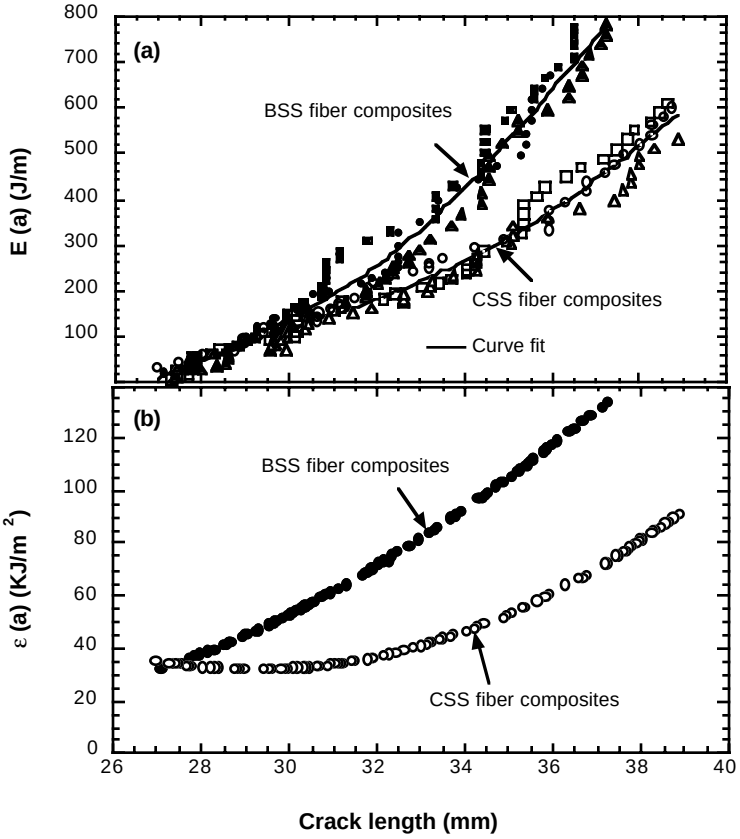

Fig. 8 (a) The total normalized energies, E(a) as a function of crack length for DCB tests of both BSS- and CSS-fiber composites with ℓ = 3 mm. The solid and hollow markers represent data points for BSS- and CSS-fiber composites, respectively; (b) the supplied energy for a crack to propagate by a unit length, ε(a), as a function of crack length.

Figure 9 shows optical photographs of crack surfaces for DCB specimens made of (a) BSS- and (b) CSS-fiber composites. River marks on the crack surfaces reveal two distinct regions for both specimens. Region I on the left side of the dark marking line is relatively flat. The river marks suggest that this region was formed by the extension of the initial crack. Region II shows local hills and valleys resulting from local crack formations and coalescence. In this region the crack propagated by coalescing with small microcracks formed in front of the main crack.

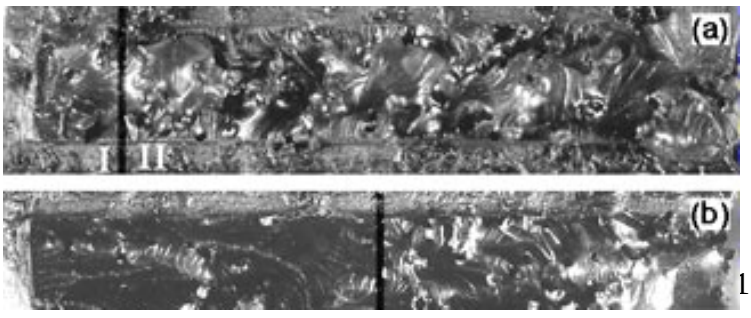

Fig. 9 Optical photographs of crack surfaces for DCB specimens made of (a) BSS- and (b) CSS-fiber composites.

Region I in the DCB specimen made of BSS-fiber composite is much shorter (< 2 mm) than that made of CSS-fiber composite (about 8 mm). This suggests higher crack-bridging capability of BSS fibers. In the BSS fiber composite, the precrack extended itself under increasing load, circumvented the BSS fibers and created a large bridging zone. As the load increased further, the main crack was effectively bridged by the BSS fibers so that it could not extend itself, and high enough stresses were produced to initiate local small cracks in front of the main crack. The crack propagation mechanism then switched to the coalescence of the main crack with these small microcracks in front of it, forming region II. Since the location and orientation of local cracks usually did not coincide with that of the main crack, the crack surfaces were roughened by crack coalescence, the process of which consumed additional energy.

3.4 Single Fiber Pullout

Single fiber pullout tests were performed to compare the crack bridging capability of a BSS fiber with a CSS fiber, to estimate the interfacial shear strength, τ_{ISS}, sliding resistance, τ_y, and critical local displacement at which the fiber end debonded from the matrix. Figure 10 shows the load (F) versus pull-out displacement (u) curves of both BSS and CSS fibers for two different embedded lengths, 3.5 mm and 6.4 mm. The free length, L_0 = 20 mm, was the same in both cases. For these embedded lengths, the fiber was fully pulled-out and did not break.

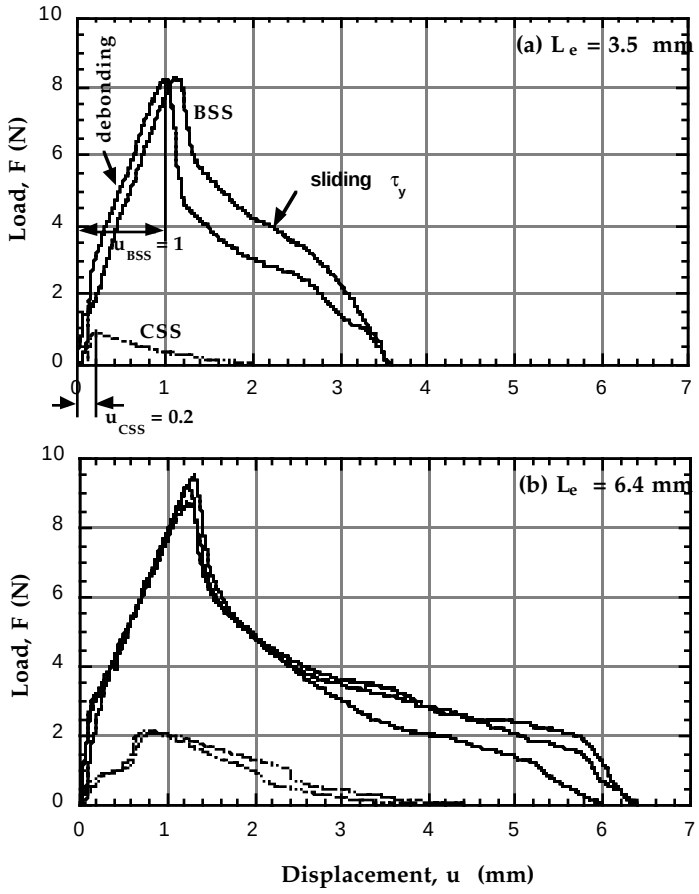

Fig. 10 The load-displacement pullout-curves of both BSS and CSS fibers for (a) the embedded length L_e = 3.5 mm and (b) L_e = 6.4 mm.

In all cases, the peak load, F_{max}, and energy consumption for pulling out a BSS fiber are much higher than those for pulling out a CSS fiber. For the pullout tests with embedded fiber length L_e = 3.5 mm (Fig. 10a), F_{max} for pulling out a BSS fiber is 9 times that for pulling out a CSS fiber. When L_e was increased from 3.5 mm to 6.4 mm (Fig. 10b), F_{max} for pulling out BSS fibers increased by only 10%. In contrast, F_{max} for pulling out CSS fibers increased by more than 150%. The total energy consumed during fiber pullout, or the area under these load-displacement curves, also increases with L_e, following a trend similar to that observed for F_{max}. For L_e = 3.5 mm, the BSS fiber consumed 17 times more energy than the CSS fiber. When L_e was increased from 3.5 mm to 6.4 mm, energy consumption increased by 70% for BSS fibers, as compared with 400% for CSS fibers.

The substantial difference in the effect of L_e between the CSS and BSS fibers on F_{max} and energy consumption is due to the difference in their pull-out failure mechanisms. The CSS fiber response depends primarily on the fiber-matrix interface integrity, which results in much more dependence of F_{max} on L_e. Increasing L_e will increase F_{max} because of the increased fiber-matrix interface area associated with debonding. In contrast, the BSS fiber response depends on its enlarged end, which directly leads to a higher F_{max} prior to the extraction process. The contribution from increasing L_e or interface area is relatively small as compared to that associated with mechanical locking of the enlarged BSS fiber end with the matrix. However, these results suggest that these relative differences between the BSS and CSS fibers will decrease with increasing L_e.

The analysis of this experiment to obtain reliable τ_y values for straight fibers is difficult and has been approached in several ways (see for example, [25-27]). Results have been shown to depend on L_0, L_e, Poisson's ratio and thermal mismatch, as well as fiber and matrix material properties. Readers are referred to [28,29] for methodologies to obtain interface characteristics in multifiber composites. For simplicity, we consider the first sign of deviation from linearity (or initial elastic response) to correspond to initiation of adhesion failure, or when the shear stress locally exceeds the interfacial shear strength τ_{ISS}. The *F-u* curve continues to

rise as the debonding crack propagates along L_e. The subsequent decay in F with further pull-out displacement u corresponds to the process of fiber extraction when the fiber (including its end) is fully debonded from the matrix. In this region, a simple shear-lag approximation [16,26] dictates that the *average* sliding shear stress obtained from experimental F-u curves is

$$\tau_y = \frac{dF}{du}\frac{1}{2\pi r} \tag{7}$$

However, the pull-out portion of these F-u curves do not have a constant slope, and so dF/du is calculated near the end of pull-out (where the effects of Poisson and thermal coefficient mismatch is minimal [26]). Using Eq. 7, rough estimates for τ_y for the L_e = 3.5 mm BSS and CSS fibers were 11 MPa and 7 MPa, respectively.

The F-u curves shown in Fig. 10 demonstrate that the potential of BSS fibers in improving composite strength and toughness are far from being fully utilized in the BSS fiber composites fabricated in this investigation. To compare pull-out results with fibers embedded in the composite wherein the stress is applied at both fiber ends, we consider $2L_e$. First of all, since the fiber did not fracture, we suspect that the $2L_e$ = 7.0 mm and 12.8 mm considered were less than ℓ_c (Eq. 3), defined by the sliding characteristics of the interface, fiber shape, and fiber strength. Secondly, the matrix did not fracture, leading to a higher effectiveness of the BSS fiber than when in the composite. For example, the highest ratio of actual effective stress of BSS fiber to the effective stress of CSS fiber is 2.58 (Table II) for ℓ = 4.5 mm. This is far below the peak load ratio of BSS fiber to CSS fiber shown in Fig. 10a, which is about 9 in the L_e = 3.5 mm case or equivalently in the composite, ℓ = 7.0 mm. Lastly, to use the values of τ_y estimated by Eq. 7 for L_e = 3.5 mm in subsequent modeling, we consider a CSS and BSS fiber composite in which ℓ = 7.0 mm.

3.5 Discussion of Fiber Geometry and Matrix Selection

BSS-fiber composites failed mostly by initiation of cracks at the enlarged fiber ends and their coalescence. This was due to a combination of factors, including the crack sensitivity of the polyester matrix, the geometry of BSS fiber ends, and interaction among these fiber ends. The mushroom-shaped geometry of the BSS fiber ends (Fig. 11a) causes tensile stress concentrations in the matrix near the mushroom edge, which can subsequently lead to crack initiation. The ends of BSS fibers promoted crack formation more severely than CSS fibers, resulting in earlier formation of cracks in the BSS-fiber composites This led to less elongation to failure in BSS-fiber composites than in CSS-fiber composites (see Fig. 6). In contrast, in the pullout tests the single BSS fiber was pulled out without cracking the matrix, and the BSS fibers were several times more effective than in the composites fabricated in this study.

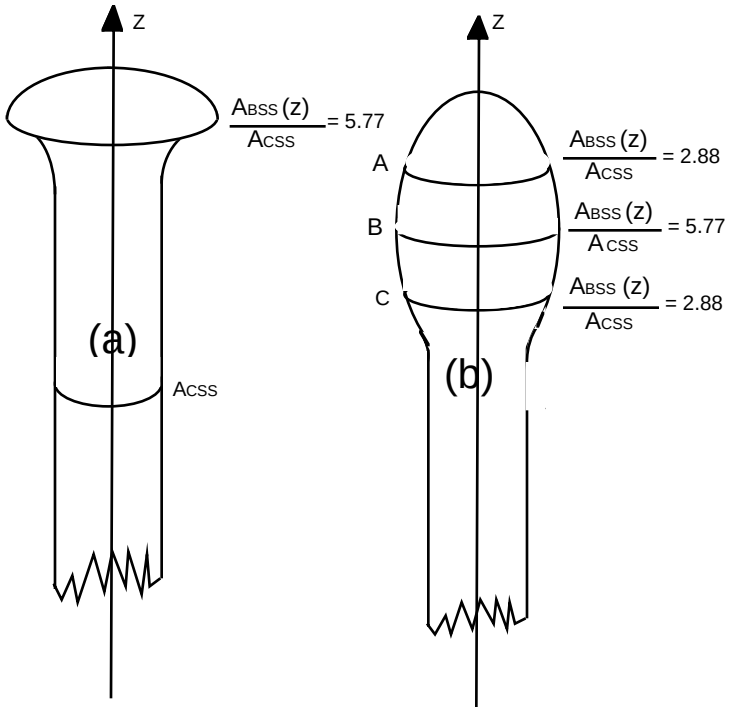

Fig. 11 (a) The disk-shaped geometry of a BSS fiber fabricated in the current study promotes crack formation in the matrix, and (b) an ideal ellipsoid geometry for BSS fibers to reduce crack formation.

For these reasons, we believe that only a small portion of the strengthening potential of BSS fibers was realized in this study. To suppress crack formation, the tensile stress concentration in the matrix near the fiber ends can be reduced by modifying the geometry of BSS fiber ends. For example, an ellipsoid fiber end, such as the one shown in Fig. 11b, will certainly result in lower stress concentration than the mushroom-shaped geometry (Fig. 11a). Also an optimized BSS fiber end and interface characteristics would allow a BSS fiber to be pulled out before the fiber stress can grow to exceed the fiber strength. Such a pullout process will increase the overall composite work of fracture, thus making full use of the potential of BSS fibers for improving fracture toughness of composite materials. Also the increase in the number of BSS fibers bridging matrix cracks rather than initiating them, would improve composite strength.. Experimental studies on optimum short fiber geometry, which will depend on fiber type, interface, and matrix properties, such as yield strength, plasticity, and crack sensitivity, will be pursued in the near future. Design of these experiments can be guided by computational modeling, as discussed in the next section.

4. Modeling Approach and Results

A physical model was developed to represent crack propagation in short fiber composites from an initial notch. Using the computational implementation of the model, we can investigate how short fiber length, morphology, elastic properties, strength distribution, and volume fraction and also the interface properties, control composite strength and toughness. In this section, we briefly introduce the model and the essential aspects of the computational algorithm. We refer the reader to Beyerlein *et al.* [30,31] for more details. For the scope of the present study, we develop the model to simulate crack propagation and use the DCB experimental results to qualitatively validate predictions. We also reserve application of this model to design issues for future work [31].

4.1 Model Composite

The model of a composite first assumes a relatively large initial notch and n_s short fibers laid out ahead of this notch and oriented perpendicular to the notch plane, $z = 0$, as shown in Fig. 12. The short fibers are assumed to have equal (surface-to-surface) spacing h, diameter $d = 2r$, Young's modulus E, and length ℓ, but to vary randomly in their axial location. Also, the cross-section of the CSS fibers is circular with area, $A_{CSS} = \pi r^2$ and is constant along the fiber axis. The cross-section of the BSS fibers is denoted as $A_{BSS}(z)$, varying along the fiber length forming a dogbone shape shown in Fig. 11b. In the random assignment of fiber location, we restrict each short fiber to intersect the crack plane, $z = 0$, somewhere along its length. The fiber end on the $z > 0$ half plane is marked end "1" and the fiber end on the other side, $z < 0$, is marked end "2". Also in this model, a far field axial load per fiber, $P\infty$, is applied. For E, G, d, and A_{CSS}, indicated in Fig. 11a, we use properties given in Section 2. We set $h = 10d$ as estimated from Figs. 4 and 5. We also show the integer indexing of fibers in Fig. 12. The initial notch or precrack a_0 is represented by a row of N contiguous fiber breaks aligned along $z = 0$ and spanning fibers $-N \le n \le -1$. The continuum crack length can be related to these N breaks by $a_0 \approx [N + 1](d+h)$. The n_s short fibers, which lie ahead of the crack, span fibers $0 \le n \le n_s - 1$. Statistical variation in the location of short fiber i, where $i = 1, \ldots, n_s$, is simulated by randomly placing one end of the fiber at $z^1{}_i = \ell u_i$ and the other at $z^2{}_i = \ell(u_i - 1)$, as shown in Fig. 12. The value of the uniform random variable, u_i, lies between 0 and 1 and is obtained from a random number generator for every i. Both the CSS and BSS fibers are of the same length $\ell = 7.0$ mm.

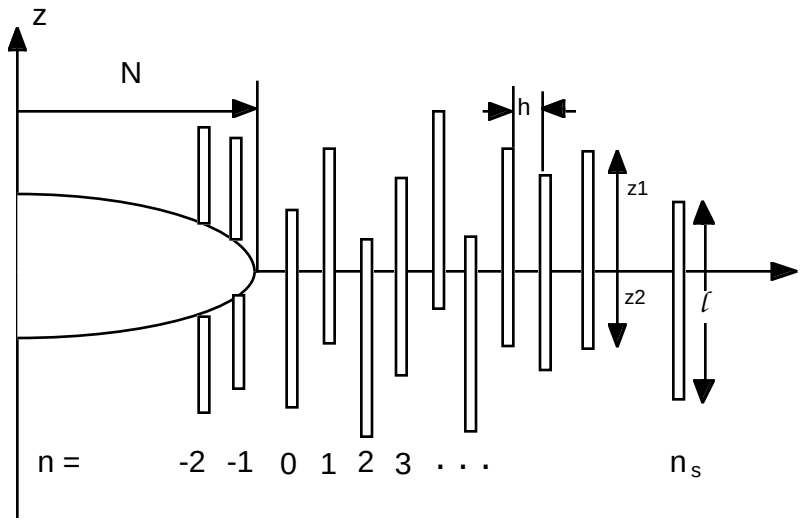

Fig. 12 Model CSS fiber composite with n_s aligned short fibers ahead of an N-sized fiber break crack.

The code uses a 2D break influence superposition (BIS) technique [32] to calculate the complex stress fields as a result of these numerous short-fiber ends coupled with a through-thickness notch. The BIS technique is an extension of the Hedgepeth 2D multifiber composite shear-lag model [33] to account for out-of-plane locations of fiber breaks. Using the BIS technique, the stress redistribution around an arbitrary configuration of fiber break locations can be calculated quite efficiently and directly. The computational effort depends jointly on the number of breaks and the size of the region one wishes to use to calculate stress and displacement. The technique is based on continuum theory so the fiber and matrix are not discretized and thus, stress redistribution results do not depend on the fineness of a mesh. The spatial extent of the stress transfer from broken to intact fibers depends on the properties of the composite and number of fractures. For a row of 50 or more fiber breaks, this Hedgepeth shear-lag model produces stress distributions

consistent with those predicted by plane elasticity theory for an orthotropic sheet containing a through-thickness crack [30]. For this reason, we consider a notch consisting of N = 50 fiber breaks.

The model also assumes that the fibers sustain all axial stress, with Young's modulus E, and the matrix deforms only in shear, with shear modulus G. This assumption is valid for the composite material system considered here, since the matrix-to-fiber stiffness ratio $E_m(1-V_f)/EV_f$ = 0.135. Also this analysis assumes that the fibers and matrix are linear elastic and well-bonded. In the original BIS technique, the effects of sliding of the fiber-matrix interface were not considered, but are included in the present model in an approximate manner, similar to that described in Zhou and Curtin [34]. Moreover, the usual boundary condition in the BIS technique is that all break surfaces are traction free; however, in this short fiber model, we introduce 'virtual' breaks, which are simply fractures sustaining nonzero, nonnegative tractions. These virtual breaks are used to model the enlarged and round BSS fiber ends and also all short fibers which are sliding and pulling-out of the matrix [31].

4.2 Local Failure Criteria

An inhomogeneous stress state is generated under loading, due to interactions between the randomly spaced fiber ends. Tensile and shear stress concentrations can promote microcrack formation at the fiber ends and subsequent sliding at the fiber/matrix interface. Short fibers remain intact during the fracture process and the macroscopic response is thus dominated by fiber bridging and pullout. All these features seen experimentally are thus incorporated into the computational model. To accurately represent the experimental results, we need the limiting shear stress at which the fiber/matrix interface separates, the interfacial shear stress for when the fiber is sliding relative to the matrix, and the critical displacement at which fiber ends separate from the matrix.

The limit shear stress or interfacial shear strength, τ_{ISS}, may be obtained from pull-out experiments. However, in Section 3.4, only an estimate for the sliding shear stress τ_y was obtained for the BSS and CSS fibers from pull-out tests with L_e = 3.5 mm, which is equivalent to an *in situ* composite length of ℓ = 7.0 mm. Since accurate estimates of τ_y and τ_{ISS} were not possible for the current polyethylene fiber model systems and also since we wish to reduce the parameter space, we assume $\tau_y = \tau_{\mathrm{ISS}} = \tau$. In the CSS case, we compare the shear stress at both tips of the fiber, $\tau_n(z^{1,2})$, with τ_{CSS} = 7 MPa. The CSS fiber ends are known to experience the highest shear stress concentration. In the BSS fiber, FEM calculations and our shear-lag calculations show that the highest shear stress occurs between the fiber tip and the middle of the spherical end [35]. Therefore, in this case, the shear stress τ_n at point A in Fig. 11b of the BSS fiber end is compared with τ_{BSS} = 11 MPa.

The bond between the fiber end and matrix are assumed to be intact until a critical displacement is reached. Full separation of the fiber end from the matrix and thus, the process of pull-out is assumed to begin at the maximum of the F versus u curves in Fig. 10. Specifically, the F-u curve in Fig. 10a for L_e = 3.5 mm was used to estimate the critical displacements corresponding to F_{max}, u_{BSS} and u_{CSS}, as 0.2 mm and 1.0 mm, respectively.

4.3 Simulation Algorithm.

In all simulations, the far field tensile load is increased to levels required to cause at least one failure event. Each crack propagation simulation occurs in discrete increments and finishes when a crack propagates through all the short fibers and they all become fully extracted. At the end of each increment, there is a change in the failure 'configuration' (i.e. a

newly debonded fiber end, pulled-out fiber, etc.), such that a recalculation of the stress redistribution and displacements is necessary. Therefore, at every increment, the stress redistribution is recalculated using BIS. In all the BIS calculations, equilibrium and compatibility are satisfied [30].

Each end of a short fiber can either be (i) fully intact, (ii) debonded from the matrix, or (iii) sliding with respect to the matrix. If at least one of the two ends of the short fiber satisfies the failure criteria corresponding to both (ii) and (iii), then this fiber is considered either (iv) pulling out but still 'bridging' the crack face or (v) completely pulled out of the main crack. This fiber is pulled out of the crack if the opening displacements of the fiber end being extracted, marked 1 or 2, exceeds z^1 or z^2, respectively.

The amount of crack extension, Δa_c, is defined from the length of contiguous fully extracted short fibers n_c starting from the initial notch. Similarly, Δa_b, is defined from the length of contiguous 'bridging' fibers (or fibers in the process of pulling out) and fully extracted short fibers n_b starting from the initial notch. Explicitly, $\Delta a_c = n_c(h+d)$ and $\Delta a_b = n_b(h+d)$.

4.4 Modeling Results

Figure 13 compares the opening displacement (CTOD) at the mouth of the initial notch versus the amount of crack extension, $\Delta a_c/(h+d) = n_c$, for the BSS and CSS fiber composites, where $N = 50$, $n_s = 75$ and $\ell = 7.0$ mm. For each type of short-fiber composite, five CTOD versus n_c curves are shown, representing five composites with different random fiber spatial distributions. Plots of normalized applied load $\overline{P}$ versus Δa_c or Δa_b show similar trends. Prior to or at initial crack extension, many failure mechanisms, such as fiber end detachment and fiber sliding can occur ahead of the initial notch. Variation between the BSS- or the CSS-fiber composite curves is due solely to the statistical variation in locations of short fiber ends with respect to the crack. Also the sharp rise in CTOD as the crack propagates to a length n_c ~60-70 is due to boundary constraints provided by the intact fibers, i.e. fibers $n > 75$. This boundary effect also occurs in the DCB specimens. We will neglect this response due to the boundary effect when comparing the BSS- and CSS-fiber composites.

Figure 13 reveals the effectiveness of the BSS fibers. Prior to the sharp rise at the end, the CTOD of the CSS-fiber composites does not increase appreciably above the short fiber length, ℓ = 7.0 mm. However, a much larger (approximately 2.5 ~ 3.0 times larger) CTOD is required to drive crack extension and complete pull-out in the BSS-fiber composites than in the CSS-fiber composites. Also, although it appears that the variation in the response of the BSS-fiber composite is much larger, the coefficient of variation, or standard deviation to mean ratio, in the CTOD of the BSS-fiber composite at n_c ~60 is slightly smaller (0.2902 versus 0.3032 for the BSS and CSS-fiber composites, respectively). This suggests that the CSS- and BSS-fiber composites have the nearly the same sensitivity in crack propagation to variation in fiber spatial distribution.

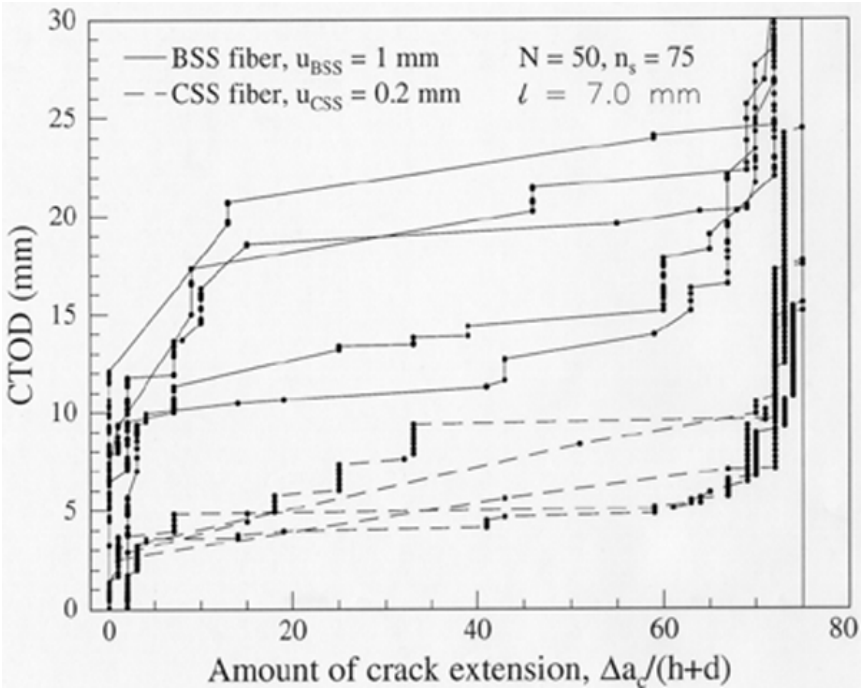

Fig. 13 Simulation predictions for the opening displacement (CTOD) at the mouth of the initial notch versus crack extension in five different BSS and CSS-fiber composites with the same short fiber length ℓ = 7.0 mm.

To reveal the damage occurring ahead of the growing Δa_c or Δa_b, graphic 'snapshots' of an increment in the simulation for a CSS and a BSS-fiber specimen at approximately the same far field normalized load (~17) are shown in Figs. 14a and b, respectively. Short fiber

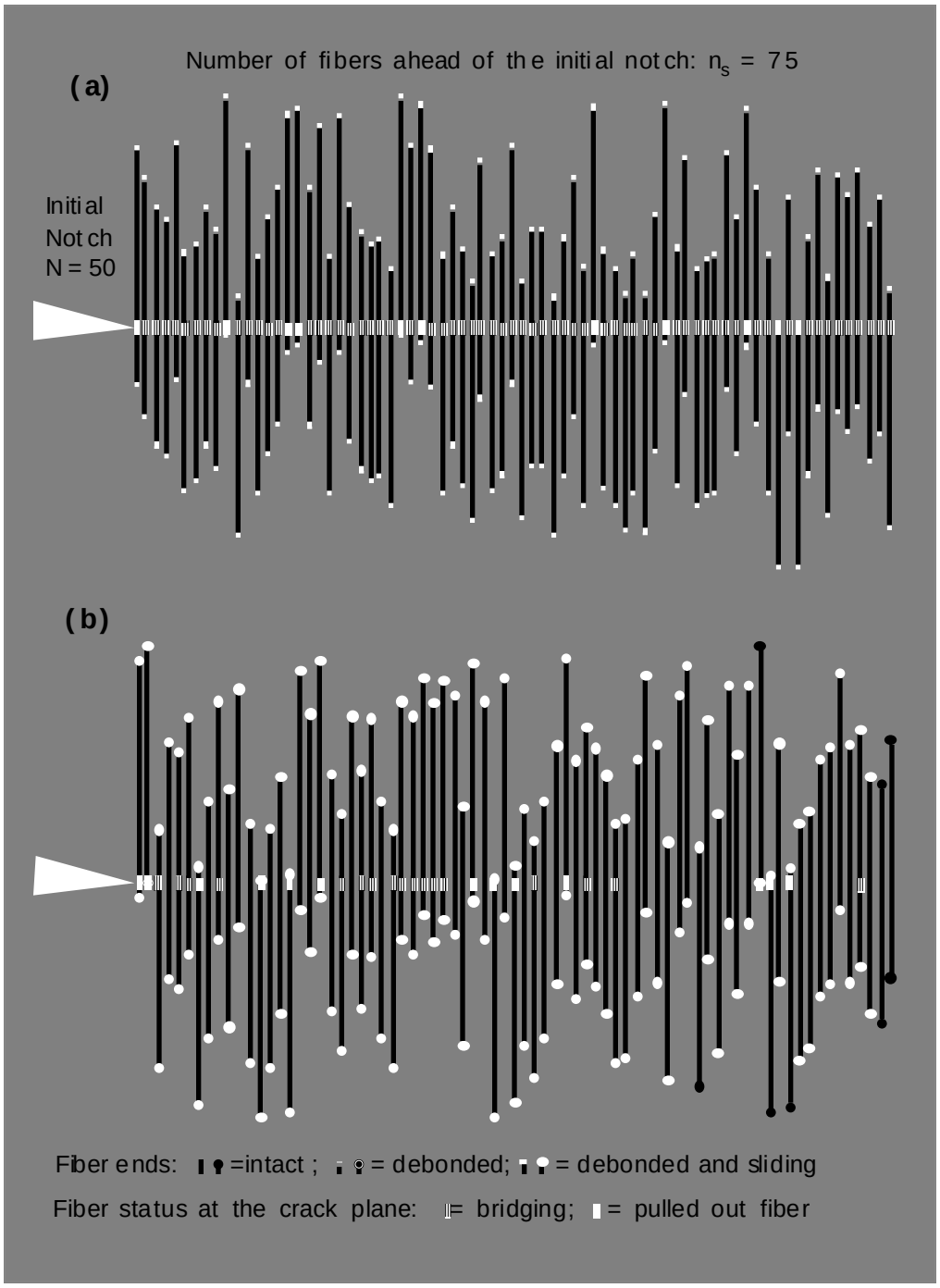

Fig. 14 An increment in crack propagation of (a) a CSS fiber composite at normalized applied load = 16.58 and (b) a BSS fiber composite at normalized applied load = 16.91. In (a) the crack extension $\Delta a_c = 1$ and $\Delta a_b = 75 = n_s$, and in (a) $\Delta a_c = 2$ and $\Delta a_b = 3$.

ends are in three states: (i) an intact end, (ii) a debonded fiber end, and (iii) a sliding fiber end, respectively. On the crack plane, $z = 0$, the fiber status is represented by two states: (iv) bridging (at least one sliding and debonded end) and (v) pulled-out short fibers, respectively. At this value of $\overline{P}$, the matrix crack in the CSS-fiber composites has already propagated to the end and contains a majority of pull-out fibers. The BSS fiber composite, on the other hand, contains a relatively smaller bridging zone at this applied load and, in general, contains both bridging and pulled-out fibers. Note that there are also a number of fibers ahead of the crack that have already satisfied the debonded, sliding, or fully extracted criteria. These fibers may have ends which are clustered near the crack plane. In these cases, the stress concentrations from the approaching crack most often promote premature microcracking in these areas, even if they are far from the crack-tip. When encountered by the approaching crack, these areas will lead to immediate crack extension or discrete steps in $\overline{P}$ vs a_c or a_b curves. Results from this simulation code are consistent with trends observed in DCB specimen tests.

5. Conclusions

Short-fiber composites reinforced with bone-shaped fibers have proven to have both higher strength and toughness than conventional short-fiber composites. By using mechanical interlocking at fiber ends to transfer load, BSS fibers allow a weak fiber/matrix interface to be used without compromising the effectiveness of load transfer. This avoids the dilemma in designing CSS-fiber composites, in which a weak interface results in low strength because of ineffective load transfer and a strong interface results in low toughness because of stress concentration.

Interfacial debonding along a BSS fiber does not affect its load carrying capability, making BSS fibers more effective than CSS-fibers in bridging a crack. This leads to higher fracture toughness for BSS-fiber composites. Another factor which contributed to enhancing the effects of the BSS fibers is the fact that the fibers used in these composites did not fracture. This is because the BSS fiber ends are not large enough to prevent the fiber from being pulled out before it is broken. The critical size of BSS fiber ends that govern the transition from a fiber being pulled out to being broken is influenced by the mechanical properties (e.g. strength, strain-to-failure), shape, and length of the fiber and the properties of the matrix and interfaces.

The crack sensitivity of the polyester matrix has played a major role in crack formation in the BSS-fiber composites fabricated in this study. The mushroom-shaped geometry of BSS fibers, coupled with the high crack sensitivity of the polyester matrix, led to the failure of BSS-fiber composites primarily by crack initiation and coalescence. This mode of failure can only utilize a small portion of the reinforcing and crack bridging potential of BSS fibers. Although the matrix in bulk can sustain large plastic strains, it behaves more like a brittle material once a crack has formed, as evidenced by the river marks on the fracture surfaces of composite specimens (Figs. 4 and 5). Therefore, we propose that ellipsoidal fiber ends and a less-crack-sensitive matrix (still providing a relatively weak interface) will suppress crack formation and further increase the strength and toughness of BSS-fiber composites. Overall, the results presented here show that it will be worthwhile to develop commercial BSS-fiber reinforced composites with weak interfaces, test their mechanical properties, and perform computational modeling for optimum fiber shape and length.

Predictions from this computational model will be used (i) to design further experimental studies, (ii) to determine the dominate failure mechanisms, (iii) to study the isolated or synergistic effects of specific parameters, and (iv) to optimize the selection of parameters to evaluate experimentally. For the present material system, volume fractions, and short fiber lengths, the fibers did not break under monotonic axial tension in either the tensile or

cantilever beam specimens. Strength was dominated by fiber end cracking and fiber pull-out. Thus, in the algorithm used in this computational model, a criteria for debonding was included, but one for fiber failure was not. However, future work will involve assigning Weibull flaw strengths randomly along the short fiber lengths. When doing so, one can determine the relationship between the critical fiber length (length at which composite failure mode becomes dominated by fiber fracture) and composite material properties, such as τ, Weibull fiber strength, and BSS-fiber morphology.

Acknowledgments

The authors acknowledge the support provided by the Laboratory Directed Research and Development Office of Los Alamos National Laboratory. IJB is grateful for the support provided by the Center for Materials Science, the Structural/Properties Relationships Group, and a J. R. Oppenheimer Fellowship. This work was performed under the auspices of the U.S. Department of Energy.

References

1. P.E. Chen, *Polymer Eng. and Sci.*, **11,** 51 (1971).
2. P.K. Liaw, J.G. Greggi, and W.A. Logsdon, *J. Mater. Sci.*, **22**, 1613 (1987).
3. S.K. Gaggar and L.J. Broutman, *Polymer Eng. and Sci.*, **16**, 537 (1976).
4. J.V. Milewski, Concise Encyclopedia of Composite Materials, revised edition, A. Kelly, Ed. p. 313, Elsevier Science, Ltd., Oxford, England (1994).
5. T.F. Klimowicz, *J. of Metals*, **November**, 49 (1994).
6. Y. Takao, Recent Advances in Composites in the United States and Japan, ASTM STP 864, J.R. Vinson and M. Taya, Eds. p. 685, ASTM, Philadelphia (1985).
7. A. Crasto, S.H. Own, and R.V. Subramanian, Composite Interfaces, H. Ishida and J. L. Koenig, eds., p. 133, Elsevier Science Publishers, New York (1986).
8. M. Fishkis, J.R. Yeh, and K. Wefers, *J. Mater. Sci.*, 29**,** 110 (1994).
9. E.A. Feest, *Composites*, **25,** 75 (1994).
10. S.M. Kunz, K. Chia, C.H. McMurtry, and W.D.G. Boecker, Composite Applications, T.J. Drozda, ed., p. 38, Society of Manufacture Engineers, Dearborn, Michigan (1989).
11. C.M. Friend, *Scripta Metall*., **23**, 33 (1989).
12. K. Xia and T.G. Langdon, *J. Mater. Sci.*, **29**, 5219 (1994).
13. Y.T. Zhu, G. Zong, A. Manthiram, and E. Eliezer, *J. Mater. Sci.*, **29**, 6281 (1994).
14. E. Yasuda, T. Akatsu, Y. Tanabe, and Y. Matsuo, Composite Materials, A. T. Benedetto, L. Nicolais, and R. Watanabe, eds., p. 167, Elsevier Science Publishers, New York (1992).
15. T. Norita, J. Matsui, and H.S. Matsuda, Composite Interfaces, H. Ishida and J. L. Koenig, eds., p. 123, Elsevier Science Publishers, New York (1986).
16. A. Kelly and W.R. Tyson, *J. Mech. Phys. Solids*, **13**, 239 (1965).
17. Y.T. Zhu, J.A. Valdez, N. Shi, M.L. Lovato, M.G. Stout, S.Zhou, B.R. Blumenthal, and T.C. Lowe, "A Composite Reinforced with Bone-Shaped Short Fibers," *Scripta Materialia* (in press).
18. B.L. Zhou, *J. of Metals*, **February**, 57 (1994).
19**.** Y.T. Zhu, W.R. Blumenthal, and T.C. Lowe, *J. Composite Materials*, **31**, 1287 (1997).
20. Y.T. Zhu, W.R. Blumenthal, and T.C. Lowe, *J. Mater. Sci.*, **32**, 2037 (1997).
21. H. Fukuda and T.W. Chou, *J. Mater. Sci*., **16**, 1088 (1981).

22. R.W. Hertzberg, Deformation and Fracture Mechanics of Engineering Materials, 3rd ed., p. 26, John Wiley & Sons, New York (1989).
23. J.P. Penning, A.A. De Vries, J. Van Der Ven, and A.J. Pennings, *Phil. Mag. A*, **69**, 267 (1994).
24. D. Broek, Elementary Engineering Fracture Mechanics, 4th ed., p. 123, Kluwer Academic Publishers, Boston (1997).
25. J.W. Hutchinson and H.M. Jensen, *Mech Mater*., **9**, 139 (1990).
26. P.S. Chua and M.R. Piggot, *Comp. Sci. Technol*., **22**, 33 (1985).
27. P. Lawrence, *J. Mater. Sci*., **7**, 1 (1972).
28. I.J. Beyerlein, M.S. Amer, L.S. Schadler, and S. L. Phoenix, *Sci. Engng. Comp. Mat.*, **7**, 151 (1998).
29. J. He, I.J. Beyerlein, and D.R. Clarke, *J. Mech. Phys. Solids*, In Press (1998).
30. I.J. Beyerlein, S.L. Phoenix, and A.M. Sastry, *Int. J. Solids Structures*, **33**, 2543 (1996).
31. I.J. Beyerlein et al, Effects of Short Fiber Shape on the Toughness of Discontinuous Fiber Composites, In preparation (1998).
32. A.M. Sastry and S.L. Phoenix, *J. Mater. Sci. Lett*, **12**, 1596 (1995).
33. J.M. Hedgepeth, NASA Tech. Note D-882 (1961).
34. S.J. Zhou and W. A. Curtin, *Acta metall. mater*., **43**, 3093 (1995).
35. S.J. Zhou *et al*, Theoretical Studies of the Strength of a Bone-Shaped Short-Fiber Composite, In preparation (1998).